Research Article

Zuriel Dathan Mora-Felix, Antonio Jesus Sanhouse-Garcia, Yaneth A. Bustos-Terrones, Juan G. Loaiza, Sergio Alberto Monjardin-Armenta, and Jesus Gabriel Rangel-Peraza*

Effect of photogrammetric RPAS flight parameters on plani-altimetric accuracy of DTM

https://doi.org/10.1515/geo-2020-0189
received October 31, 2019; accepted July 17, 2020

Abstract: Remotely piloted aerial systems (RPASs) are gaining fast and wide application around the world due to its relative low-cost advantage in the acquisition of high-resolution imagery. However, standardized protocols for the construction of cartographic products are needed. The aim of this paper is to optimize the generation of digital terrain models (DTMs) by using different RPAS flight parameters. An orthogonal design L18 was used to measure the effect of photogrammetric flight parameters on the DTM generated. The image data were acquired using a DJI Phantom 4 Pro drone and six flight parameters were evaluated: flight mode, altitude, flight speed, camera tilt, longitudinal overlap and transversal overlap. Fifty-one ground control points were established using a global positioning system. Multivision algorithms were used to obtain ultra-high resolution point clouds, orthophotos and 3D models from the photos acquired. Root mean square error was used to measure the geometric accuracy of DTMs generated. The effect of photogrammetric flight parameters was carried out by using analysis of variance statistical analysis. Altimetric and planimetric accuracies of 0.38 and 0.11 m were achieved, respectively. Based on these results, high-precision cartographic material was generated using low-cost technology.

Keywords: remotely piloted aircraft systems, photogrammetry, DTM, terrain modeling, environmental management

*** Corresponding author: Jesus Gabriel Rangel-Peraza,** Division de Estudios de Posgrado e Investigacion, Tecnologico Nacional de Mexico – Instituto Tecnologico de Culiacan, Culiacan, Mexico, e-mail: jesus.rp@culiacan.tecn.mx
Zuriel Dathan Mora-Felix: Division de Estudios de Posgrado e Investigacion, Tecnologico Nacional de Mexico – Instituto Tecnologico de Culiacan, Culiacan, Mexico, e-mail: zuriel.mf@culiacan.tecnm.mx
Antonio Jesus Sanhouse-Garcia: Departamento de Tecnología Ambiental, Universidad Tecnologica de Culiacan, Culiacan, Mexico, e-mail: a.sanhouse@utculiacan.edu.mx
Yaneth A. Bustos-Terrones: Division de Estudios de Posgrado e Investigacion, CONACYT – TecNM – Instituto Tecnologico de Culiacan, Culiacan, Mexico, e-mail: yabustoste@conacyt.mx
Juan G. Loaiza: Tecnologico Nacional de Mexico – Instituto Tecnologico de Culiacan, Culiacan, Mexico, e-mail: juangabrielloaiza@gmail.com
Sergio Alberto Monjardin-Armenta: Facultad de Ciencias de la Tierra y el Espacio, Universidad Autónoma de Sinaloa, Culiacan, Mexico, e-mail: sa.monjardin12@info.uas.edu.mx

Abbreviations

ALS	aerial laser scanner
ANOVA	analysis of variance
CP	checkpoint
DEM	digital elevation model
DSM	digital surface model
DTM	digital terrain model
GCP	ground control points
GNSS	global navigation satellite system
GPS	global positioning system
GSD	ground sample distance
IMU	inertial measurement unit
INS	inertial navigation system
LIDAR	light detection and ranging
LM	levenberg-marquardt
NSSDA	national standard for spatial data accuracy
RMSE	root mean square error
RPAS	remotely piloted aerial system
SfM	structure from motion
SIFT	scale invariant feature transform
SMG	semiglobal matching
TIN	triangular irregular network
TLS	terrestrial laser scanner
UTM	universal transverse mercator
WGS	world geodetic system

1 Introduction

Digital elevation model (DEM) is a 3D graphical representation of the terrain surface, which allows

describing its morphology (digital terrain model (DTM)) and the anthropogenic elements or the vegetation present on digital surface model (DSM). DEMs provide critical data that are very useful to delineate, explain and predict any terrain surface change, especially when high-resolution spatial data are needed [1]. The technologies used to build high-precision DEMs are robotic total stations [2], global navigation satellite systems (GNSS) [3], terrestrial laser scanner [4] and aerial laser scanner [5]. Some limitations of the use of these technologies are the complexity of acquisition data, high operating costs and long working periods for acquiring high detailed information [6].

Conventional remotely piloted aerial systems (RPAS) photogrammetry is considered as an economic alternative and it is capable of extracting images to build high-detailed surface models that are very useful for scientific research [7]. Its implementation does not require many aerial images; therefore, this technology does not require complex methodological activities. According to Uysal et al. [8], RPAS photogrammetry is a robust technology for topographic mapping and modeling with several advantages such as cost reduction, easy access to complicated areas, reduced operation times and field activities, among others. This technology can compete with others that can develop high detail DEMs [9].

However, RPAS photogrammetry is sensitive to factors such as light intensity changes, photograph scale and rotations. Data acquisition is performed in a similar way as the conventional photogrammetric flights. Several studies describe the effect of RPAS flight parameter configuration on plani-altimetric precision and DEM accuracy [10–13]. Camera configuration parameters, such as angular orientation, resolution and lens diameter, are essential to obtain results with high resolution and level of detail [10–12]. However, sometimes noise can produce images with distortions. Therefore, the calibration process of the camera is also recognized to obtain high-quality images for further processing [6], but other studies are focused on the development of control algorithms to compensate the wind gusts during a flight [14,15].

Eltner et al. [9] and Hirschmüller [16] suggest that flight altitude, speed and trajectory have a greater influence on DEM accuracy. Ground sample distance (GSD) and longitudinal and lateral overlaps have also been proposed as critical flight parameters in RPAS photogrammetry [17]. However, recent studies have demonstrated that high-quality cartographic products are obtained when implementing image processing technologies such as artificial vision algorithms and artificial stereoscopic simulation [18–20]. The DEM accuracy registered when using structure from motion (SfM) for image processing in RPAS photogrammetry has already been compared with airborne light detection and ranging technology [21]. Therefore, the construction of maps and 3D terrain models through the collection and integration of photographs from different heights and directions have been proposed as an alternative to counter the discrepancies found in literature related to RPAS flight configuration [22,23].

The aforementioned studies separately analyze the effect of one or two photogrammetric parameters. Since a comparison of all these photogrammetric parameters has not been carried out at the time of being manipulated simultaneously, this study proposes a novel experimental strategy that allows analyzing the influence of six photogrammetric flight parameters by using an L_{18} orthogonal array and the implementation of artificial vision algorithms for image processing. The main objectives of this study are to assess the effect of different flight parameter configurations on DTM accuracy and figure out the optimum flight conditions where the lowest planimetric and altimetric errors are obtained.

2 Methods

2.1 Study area

The study area is located in the city of Culiacan, Sinaloa, Mexico. Specifically, in the lower part of Culiacan river basin, in coordinates 24°48′40.3″ – 24°48′69.2″ N, 107°24′ 53.1″ – 1 07°24′24.5′ W according to World Geodetic System 84 (WGS84) reference system. High-intensity rainfalls and tropical storms occur in the study area during rainy season [24]. In particular, the lower part of Culiacan river basin was selected as the study area (Figure 1). This zone is a sloping terrain characterized by constant flooding caused by the rise of the Tamazula River. These river floods have caused severe damage to the urban area. Therefore, high detail DEM is needed for future hydrological modeling in this area.

2.2 DEM construction process

The methodology used in this study is presented in Figure 2. DEM construction process was characterized by

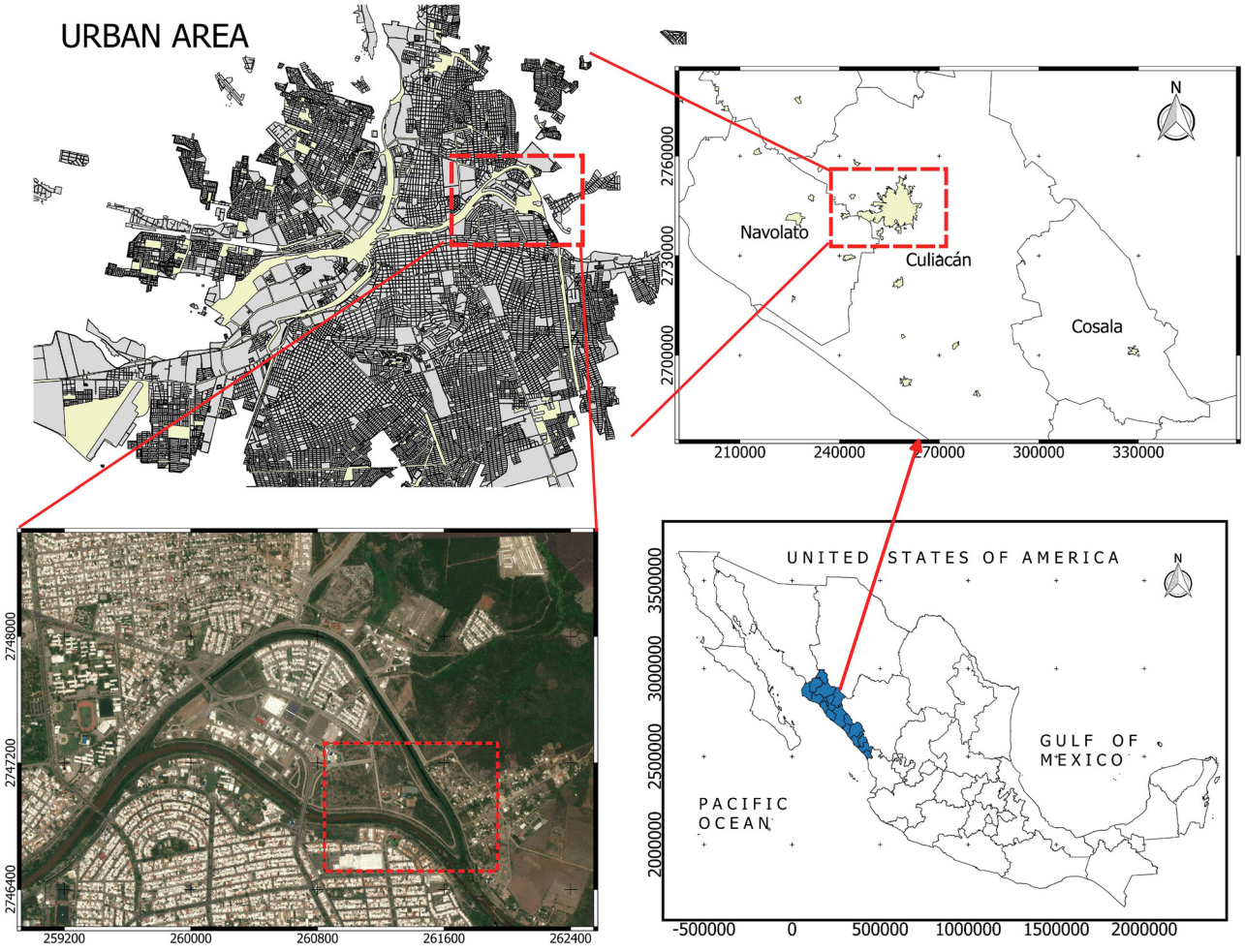

Figure 1: Study area. Source: Own elaboration using QGIS 3.10 La coruña (Open Source Geospatial Foundation, Beaverton, USA, 2020).

three main phases: the first phase consisted of photogrammetric flight planning project, where the flight parameters of RPAS were established and the photogrammetric surveys were carried out. Data processing was the second phase and consisted of defining a photogrammetric block and some information about a scene during image capturing process was obtained (i.e., camera orientation and image point correlation). At this stage, the 3D reconstruction was also carried out through the extraction process (point cloud extraction). Then, DEM generation was carried out by using different mathematical algorithms with SfM technology (SIFT, Hamming Distance, Poisson reconstruction, SemiGlobal Matching (SMG) algorithms and Delaunay triangulation). Finally, the third phase involved the DEM accuracy assessment using root mean square error (RMSE). Then, statistical analysis (analysis of variance [ANOVA]) was carried out to evaluate the effect of photogrammetric flight parameters on DEM accuracy.

2.3 First phase: photogrammetric project definition

Step 1.1 Project Definition. A Quad Copter DJI Phantom 4 Pro was used for image acquisition. This RPAS has a global positioning system (GPS)/GLONASS and a sensor mounted on a gimbal stabilizer. A Sony RX100 camera with 35 mm focal length CMOS sensor of 20.2 effective megapixels was used. The strategies used in a conventional photogrammetric flight planning were implemented in the RPAS flight. Photogrammetric project began defining the area of interest: a polygon was drawn on a geo-referenced base map, camera and sensors onboard were calibrated (tested).

Step 1.2 Flight Planning. Free areas were located as landing points of the RPAS in case of an emergency. Then, the photogrammetric parameters were defined. The RPAS parameters considered in this study were flight mode, flight altitude, flight speed, camera tilt and

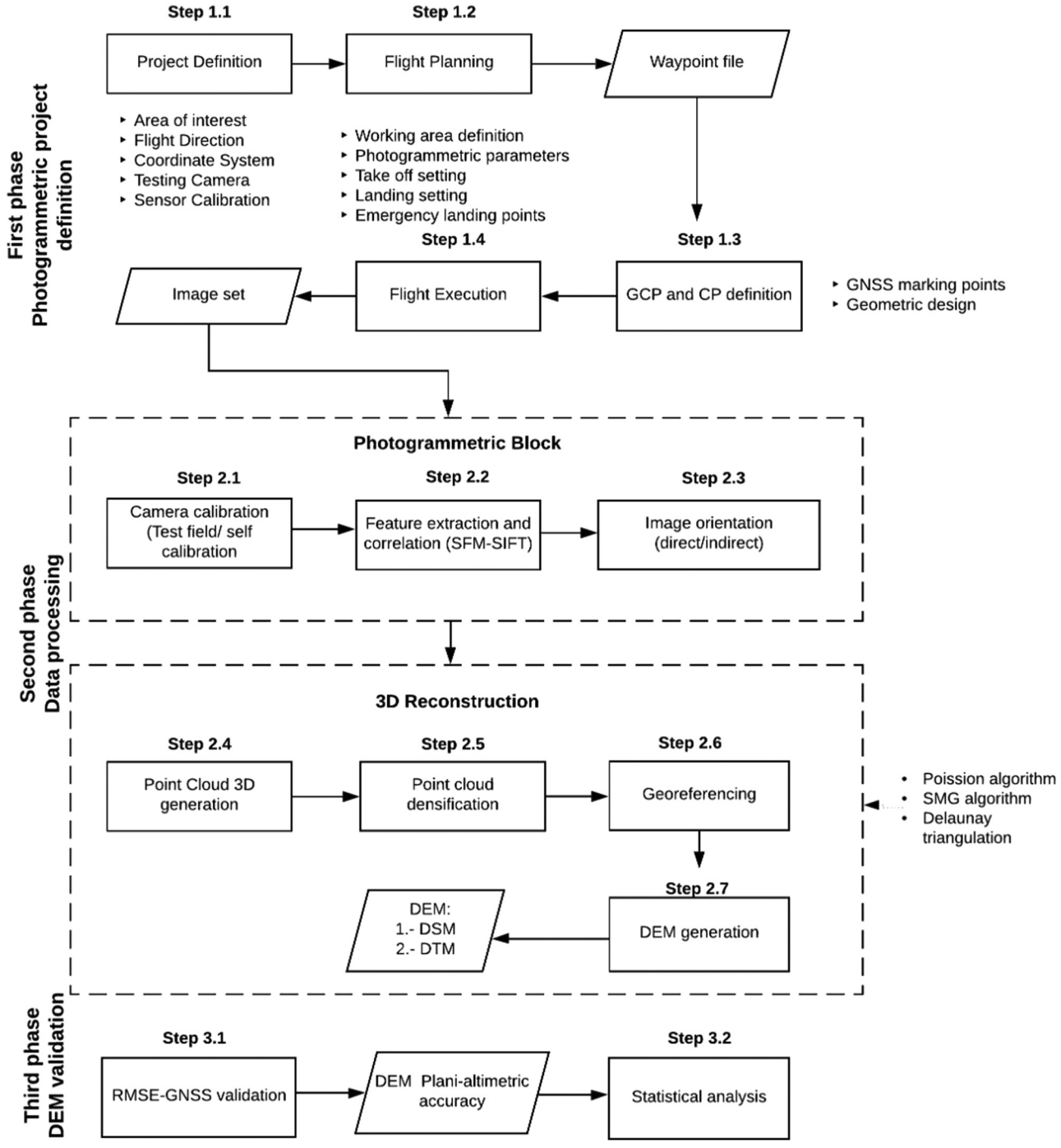

Figure 2: DEM process generation diagram. Source: Own elaboration.

the longitudinal and transversal overlaps of the images. An orthogonal array L18 was used to determine the different flight parameters for image acquisition (Table 1). This orthogonal array was used to measure the effect of these six photogrammetric flight parameters on the accuracy of DEMs generated.

According to Zhao et al. [20], a double grid flight is recommended to obtain a more accurate point cloud. In this sense, the flights were made in single and double grid. Flight altitudes were carried out at 60, 70 y 80 m as indicated by Hussain and Bethel [25]. In this study, longitudinal overlaps between 40% and 60% were

Table 1: Flight parameters used for image acquisition

Treatment	Flight mode	Flight altitude (m)	Camera tilt	Image overlap		Speed (m/s)
				Longitudinal overlap (%)	Transversal overlap (%)	
1	Normal Grid	60	65	40	60	5
2		60	75	50	70	7
3		60	85	60	80	9
4		70	65	40	70	7
5		70	75	50	80	9
6		70	85	60	60	5
7		80	65	50	60	9
8		80	75	60	70	5
9		80	85	40	80	7
10	Double grid	60	65	60	80	7
11		60	75	40	60	9
12		60	85	50	70	5
13		70	65	50	80	5
14		70	75	60	60	7
15		70	85	40	70	9
16		80	65	60	70	9
17		80	75	40	80	5
18		80	85	50	60	7

Source: Own elaboration.

defined as suggested by Reshetyuk and Mårtensson [26], while lateral overlaps between 60% and 80% were established as suggested by Harwin and Lucieer [16] and Dall'Asta et al. [27]. Under these conditions, high quality topographic maps have been reported. Regarding the camera tilt, positions close to nadir (90°) were chosen as suggested by Wasklewicz et al. [28] and Bemis et al. [29]. Oblique angular positions between 65° and 85° were also chosen. Concerning the RPAS, speed values of 3, 6 and 9 m/s were chosen to analyze distortions generated due to camera instability at high velocities.

According to Mora-Felix [30], image resolution is related to GSD. In this study, images resolution values were considered between 2 and 3 cm/pix. These values correspond to the resolutions of the most widely lightweight cameras installed on RPAS [31]. Once the photogrammetric parameters were stablished, mathematical models proposed by Vollgger and Cruden [32] and Mora-Felix et al. [30] were implemented to compute RPAS flight trajectories and programming camera shots, which are the parameters required to execute the real-time flight.

Step 1.3 Control points establishment. GNSS Trimble R10 was used for setting control points on Earth surface. This is high precision equipment that works with satellite system GLONASS, SBAS, Galileo and GPS. Each checkpoint was marked with physical signals on the ground. These marks were established before the surveys to be identified by the RPAS. Crosses in orange color were marked on the ground because they contrast with the background and are observed perfectly in the images. Control points were distributed throughout the study area as 20 × 20 cm marks to improve the triangulation and the DEM accuracy [33]. The marks were located on physical objects, such as drains, crosswalks and wood fixed to the surface by stakes were used in zones where no asphalt or concrete was present.

Step 1.4 Flight execution. During the processing of photogrammetric parameters, a file was generated containing the flight instructions that the RPAS must execute (waypoint file). This file contained GPS coordinates of a group of points that represent the photogrammetric flight to be followed sequentially by RPAS. This file also contained flight speed, flight altitude and shooting frequency configuration. Waypoint file was loaded and then the photogrammetric flight started. Through the navigation system, RPAS autonomously took position at the starting point and then automatically captured the images according to the sequence previously established. RPAS flight was monitored from a central station and furthermore an image dataset was generated.

2.4 Second phase: dataset processing

Image dataset processing was performed by SfM [34]. Image processing was characterized by two main sub-

phases: first, a photogrammetric block configuration was performed. At this sub-phase, image dataset is calibrated. Then, detection and feature correlation processes were carried out. Atypical data was eliminated and image orientation was carried out through aerial triangulation. Points relating images to each other were identified and finally the block adjustment was done.

The second sub-phase consisted of the 3D reconstruction. At this stage, disperse point cloud was generated and a densification process was performed on the point cloud. Subsequently a georeferencing process was performed and finally a triangular mesh (triangulation Delaunay) was used for the DEM generation. The dataset processing phase is fully described below:

2.5 Subphase one: photogrammetric block configuration

Step 2.1 Camera calibration. Before the flight execution, a camera calibration process was carried out. This calibration process is a fundamental requirement for the metrical reconstruction of images in photogrammetry [35]. In addition, this process reduces any alteration or noise in the cartographic product. In this study, automatic calibration was implemented as suggested by Fraser [36]. During camera calibration process, extrinsic and intrinsic parameters were obtained, which are related to the external and internal orientation processes of DEM. Extrinsic parameters refer to the coordinates in a reference system and orientation. Intrinsic parameters refer to the focal length, the central point of the image and distortions of the camera lenses. Noise was reduced by adjusting the tangential (p_1, p_2) and radial (k_1, k_2, k_3,) distortion coefficients based on Brown's distortion model [37].

Step 2.2 Feature extraction and correlation. In a photogrammetric survey with RPAS, the dataset of a photogrammetric block corresponds to the images captured during flight survey and the parameters that correlate them (overlap) with the recorded scene (position and orientation). The photogrammetric block configuration process was carried out by implementing detection and feature correlation algorithms. The most used detector algorithm in SfM artificial vision systems is the scale invariant feature transform (SIFT) algorithm [38]. This algorithm was used to extract image features. SIFT algorithm generated a set of key points between stereoscopic pairs of images that were invariant (robust) to image scale, translation, rotation and partially invariant to changes in camera illumination. The set of key points generated from images were then processed through Hamming Distance correlation algorithm [34].

Step 2.3 Image orientation. An image orientation process was applied to determine external orientation parameters (position coordinates and tilt angles) for each image. The aerial triangulation was implemented for this process. The exterior orientation elements include camera position on the platform in the coordinates x, y, z and the three angles of camera tilt (ω, φ, κ). These coordinates and angles are relative to the ground coordinate system. The positions of coordinates x, y, z were obtained by a GPS system on board. Camera angles were measured by using the INS (Inertial Navigation System) and IMU (Inertial Measurement Unit) devices. For absolute orientation, tie points (homologous points) between images were used. In addition, an image alignment process was done by using four ground control points (GCPs) defined at the corners of the model to ensure a more accurate result and eliminate the bowling effects of the RPAS data [39]. Extrinsic and intrinsic camera parameters were adjusted to perform the block adjustment procedure. Finally, Levenberg–-Marquardt (LM) algorithm was used to minimize the reprojection error. This is a robust algorithm based on the non-linear least squares method. LM minimizes the reprojection error between the observed and predicted image points [40].

2.6 Subphase two: 3D reconstruction

The 3D reconstruction consisted of four steps clearly identified: scattered point cloud generation, point cloud densification, georeferencing and DEM generation. These stages are described as following.

Step 2.4 3D point cloud generation. The coordinates of the extracted points were determined and a disparity map was computed by calculating the stereoscopic correspondence of each object. Based on this map, the distance between ground objects and the camera was obtained. The depth z of a point P(x, y, z) in a 3D reconstruction was obtained with equations (1)–(3), considering a triangular geometrical relationship.

$$I_1 = \frac{b/2 + x}{z} = \frac{x_i}{f} \rightarrow x_i = \frac{f}{z}\left(x + \frac{b}{2}\right), \quad (1)$$

$$I_r = \frac{b/2 - x}{z} = \frac{x_d}{f} \rightarrow x_d = \frac{f}{z}\left(x - \frac{b}{2}\right), \quad (2)$$

$$d = x_i - x_d = \frac{f * b}{z} \rightarrow z = \frac{f * b}{d}, \quad (3)$$

where b is the value of baseline, f is the focal length, I_l, l_r are the left and right images respectively, d is the distance from the camera to a point on the ground. Finally, the resulting data is a dispersed point cloud referred to a local coordinate system Universal Transverse Mercator, WGS84 zone 13. For this procedure, Helmert transformation was implemented [41].

Step 2.5 Point cloud densification. Consisted of extracting a larger amount of 3D points from the scene that complements the disperse point cloud generated in the previous stage. SMG was implemented due to its high precision and computational cost reduction [42]. Once the dense map was available, atypical points were eliminated (error points). Then, the Delaunay triangulation algorithm was implemented for the generation of the triangular irregular network. In this algorithm, the elevation values were interpolated (triangulated) for the generation of a regular matrix in raster format (triangular mesh) [43]. The created mesh is textured by re-projecting the 3D points with the original images to obtain the corresponding color.

Step 2.6 Georeferencing process. Before the DTM is generated, a georeferencing process is suggested. This process consisted of linking identifiable locations in the images with the locations of GCPs that were spatially related. Identifiable locations, such as sidewalks, corners, culverts, were used for georeferencing. Then, polynomial transformation was generated to adjust the locations to its correct spatial location [44].

Step 2.7 DEM generation. After constructing the triangular mesh, a smoothing model was constructed to fill the gaps in the surface and repair the errors generated. Poisson algorithm was implemented for this surface reconstruction [45]. This surface reconstruction is represented in a DSM. Finally, a Digital Terrain Model (DTM) was generated with the algorithm proposed by Unger et al. [46]. This algorithm removed man-made objects (i.e., buildings) and vegetation. Afterwards, a DTM was regularized through Huber norm.

2.7 Third phase: DEM validation

Step 3.1 RMSE-validation. DEM accuracy refers to the proximity of the observation of a coordinate point to a true value. Plani-altimetric error must be minimized to obtain a more accurate model [47]. According to National Standard for Spatial Data Accuracy, DEM errors meet a normal distribution and this is a fair assumption for open terrains [48]. In this study, DEM validation consisted of a comparison between plani-altimetric features with the GNSS points acquired in the study area. Planimetric and altimetric errors were calculated for the 18 DTMs generated. The most common statistic used to describe planimetric and altimetric errors in DEMs is the RMSE [49]. The RSME measures the difference between the values predicted by the DEM and the values observed (GNSS points).

Altimetric accuracy ($RMSE_z$) of DTM was carried out by using equation (4). This statistical parameter consists of a comparison between the elevation points obtained with GNSS and those marked on ground.

$$RMSE_Z = \sqrt{\frac{\sum_{i=1}^{n}(Z_{CP} - Z_{DTM})^2}{n}}, \quad (4)$$

In this equation, n refers to the total points measured, Z_{DTM} corresponds to the elevation of the control points marked on the ground visible in the image, Z_{CP} corresponds to the elevation of the GCP using GNSS. Planimetric validation ($RMSE_{x,y}$) was determined by the distance between the GCPs and the marked points (CPs) on the ground for both x and y coordinates. This validation was carried out using equation (5).

$$RMSE_{xy} = \sqrt{\frac{\sum_{i=1}^{n}[(X_{CP} - X_{DTM})^2 + (Y_{CP} - Y_{DTM})^2]}{n}} \quad (5)$$

where n refers to the total points to be measured, X_{DTM}, Y_{DTM} are the coordinates of the points in the model and $X_{CP}Y_{CP}$ are the coordinates of the validations GNSS points.

Step 3.2 Statistical analysis. An ANOVA was carried out to measure the effect of RPAS flight parameters on DTM accuracy ($\alpha = 0.05$). The planimetric ($RMSE_{xy}$) and the altimetric ($RMSE_z$) errors were used as response variables for this statistical analysis. ANOVA identified the flight parameters that showed a significant influence on the response variables. An optimization strategy was then carried out to find out the optimum flight configuration and to obtain the DTM with the best plani-altimetric accuracy.

3 Results

3.1 Camera calibration

Servomotors service and camera calibration were carried out to achieve the best survey performance and to avoid mechanical failures. A self-calibration process was done

Table 2: Internal parameters for camera calibration

Values	Focal length		Principal point *x*		Principal point *y*		k_1	k_2	k_3	p_1	p_2
	pix	mm	pix	mm	pix	mm					
Initial values	3073.41	4.861	1917.79	3.033	1485.8	2.35	0.033	−0.036	0.078	0	−0.001
Optimized values	3270.60	5.173	1958.79	3.098	1449.6	2.293	0.024	−0.085	−0.001	−0.001	0
Standard error	4.154	0.007	0.202	0	1.131	0.002	0	0.002	0	0	0

Source: Own elaboration using Python 3.6.5 (Python Software Foundation, Wilmington, Delaware, USA, 2011).

according to the suggested by Fraser [36]. The camera calibration parameters used in this study are presented in Table 2. The main objective of the calibration process is to solve the radial (k_1, k_2, k_3) and tangential (p_1, p_2) distortion parameters to reduce uncertainties or errors of the principal points *x* and *y*. This calibration is needed to obtain the most accurate results during the key point detection and correlation processes in stereoscopic pairs. Based on the errors obtained in this study, the calibration process could be considered as satisfactory for the 3D reconstruction process.

3.2 Ground control points and checkpoints

In this study, 51 points were established, from which 27 points (GCPs) were used for georeferencing and 24 points (checkpoints, CPs) were used for validation. Figure 3 shows the GCPs and CPs distributed in the study area.

3.3 Photogrammetric project definition (execution)

Table 3 shows the GSD, frames, areas covered and flight lines obtained in the photogrammetric surveys (treatments) that were conducted for image acquisition. Each treatment generated an average of 328 images, with a mean GSD of 2.53 cm/pix. Approximately 6,000 photographs were taken and 6.3 km were covered. It is noteworthy that a greater number of flight lines were registered in the last nine treatments. These surveys were carried out under double grid flight mode.

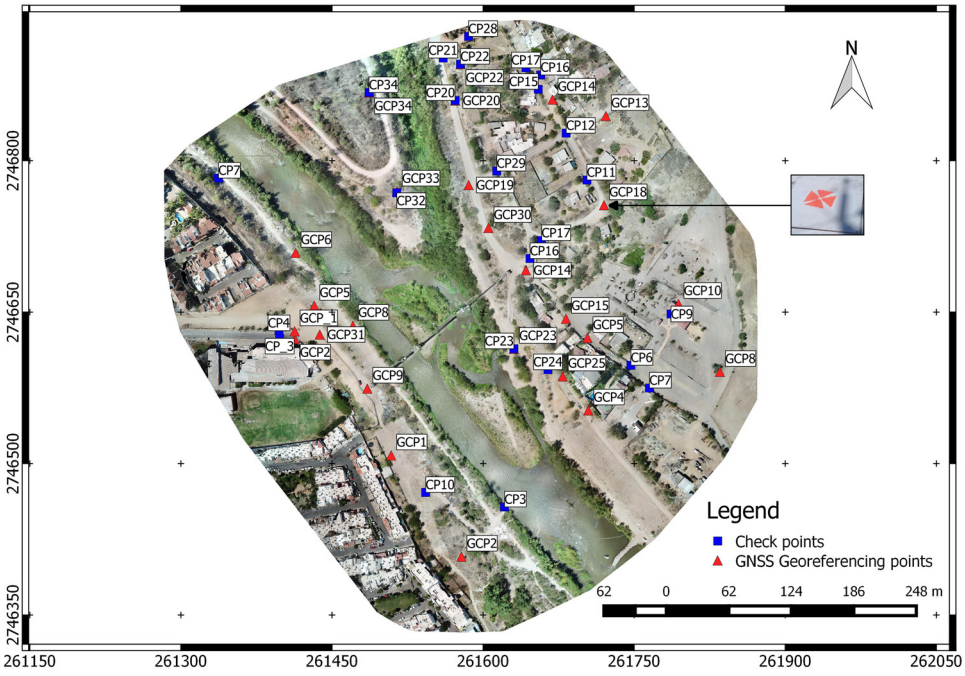

Figure 3: Location of GCPs in the study area. Source: Own elaboration using QGIS 3.10 La coruña (Open Source Geospatial Foundation, Beaverton, USA, 2020).

Table 3: GSD, frames, areas covered and flight lines obtained in the photogrammetric

Treatment	GSD (cm/pix)	Frames	Area covered (km^2)	Flight lines
1	2.38	153	0.125	11
2	2.08	215	0.158	15
3	2.55	331	0.165	12
4	2.74	143	0.178	13
5	2.39	228	0.179	19
6	2.31	150	0.164	10
7	3.08	144	0.184	9
8	2.78	143	0.183	11
9	2.15	256	0.211	16
10	2.31	881	0.228	51
11	2.01	385	0.181	26
12	2.48	526	0.222	25
13	2.67	469	0.191	37
14	2.42	377	0.119	22
15	2.51	541	0.278	20
16	2.97	362	0.256	27
17	2.81	358	0.224	38
18	2.95	257	0.278	32

Source: Own elaboration.

Likewise, it was demonstrated that the flight lines depended on the overlap of images and flight mode. It is also noteworthy that the quantity of frames acquired under normal grid flight mode is significantly smaller than the ones acquired when the double grid flights were performed.

3.4 Image processing

Figure 4 shows the results of keypoint extraction process of treatment 13 by overlapping a pair of images. In this figure, it is evidenced that most of the keypoints were correctly matched, especially in areas of dense vegetation where erroneous coincidences are possible due to the presence of similar local texture.

During the 3D reconstruction, the algorithm identified a mean of 37,336 keypoints per image (Table 4). Despite the keypoints per image were similar in all treatments, the number of match points found in double grid treatments was greater than the observed during

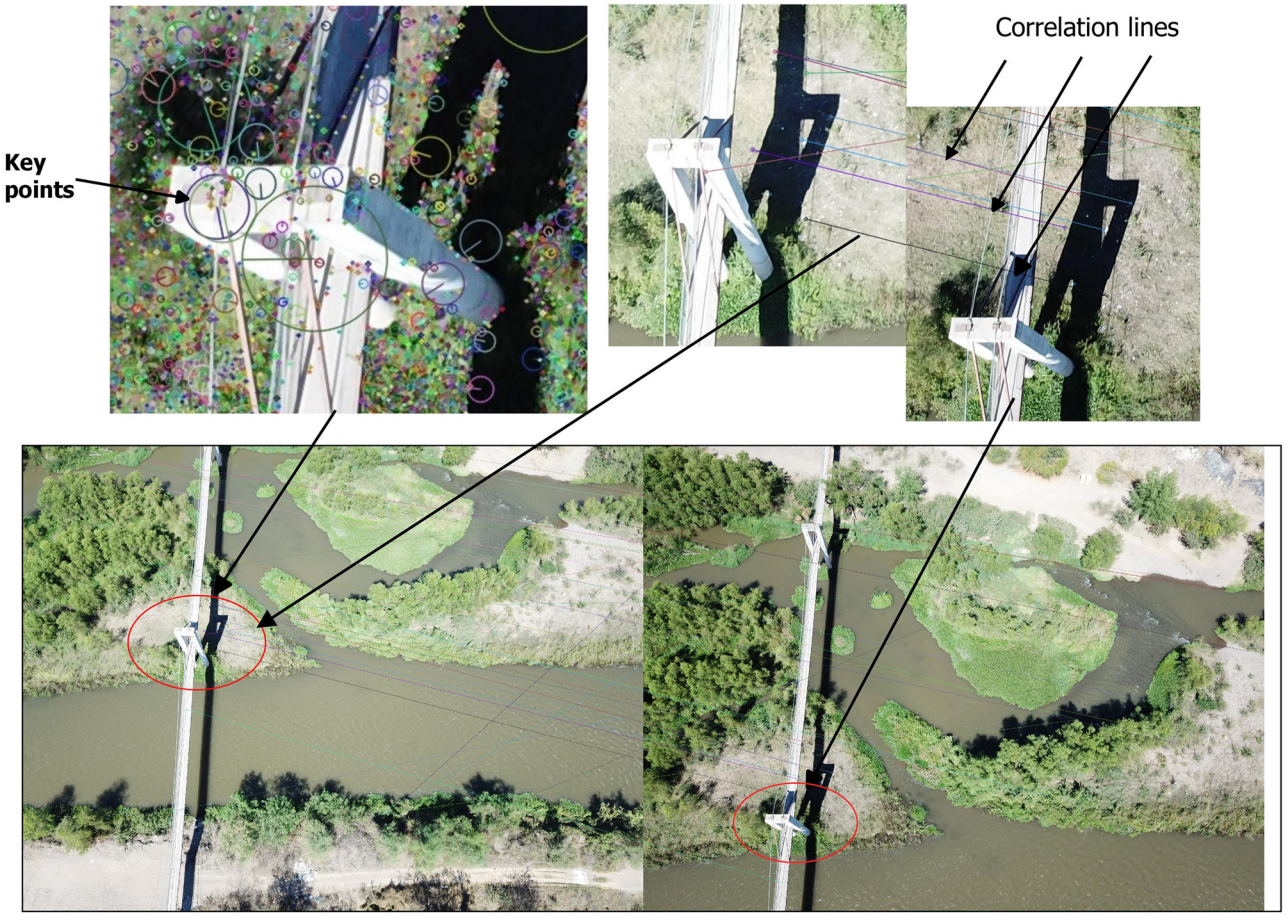

Figure 4: Keypoint detection, feature correlations and stereo pair assembling during image processing with SIFT algorithm. Source: Own elaboration using SIFT algorithm in Python 3.6.5 (Python Software Foundation, Wilmington, Delaware, USA, 2011).

Table 4: Number of key points identified and densification points obtained during 3D reconstruction

Treatment	Key points per image	Matches	3D reconstruction key point matches			3D densification points
			2 images	3 images	5 images	
1	42,631	3,292	1,49,079	14,587	5,831	46,12,634
2	40,427	4,956	3,37,297	58,225	8,974	1,38,03,790
3	44,123	5,213	34,568	78,456	1,545	1,52,36,211
4	27,127	2,620	1,39,375	17,660	1,636	73,50,091
5	30,016	4,304	2,82,627	58,711	11,183	1,56,68,844
6	32,222	5,111	2,32,080	46,436	8,969	1,17,27,625
7	30,254	3,254	1,30,117	13,232	7,675	45,08,682
8	45,220	6,889	3,22,167	57,582	8,083	1,03,23,861
9	42,858	9,245	5,99,267	1,44,033	28,962	1,91,71,283
10	38,538	2,450	640,172	1,30,146	20,372	4,77,36,416
11	38,747	5,395	6,41,806	88,598	10,246	1,70,61,978
12	37,485	5,789	678,796	87,456	10,547	1,67,56,778
13	39,226	6,129	7,35,884	1,35,396	21,601	2,53,07,000
14	34,819	5,944	5,89,488	1,04,079	14,635	1,90,89,412
15	38,795	6,456	4,78,978	1,24,568	15,478	1,78,45,681
16	37,256	6,919	8,16,464	1,43,055	18,955	2,55,85,938
17	36,675	7,056	7,55,720	1,34,660	22,464	2,34,27,473
18	35,645	7,014	8,31,254	1,56,231	45,783	2,21,34,654

Source: Own elaboration using VisualSFM [62].

normal grid. This situation could explain the fact that the number of keypoints obtained in the 3D densification process was greater when double grid flight mode was carried out.

3.5 Planimetric ($RMSE_{xy}$) and altimetric ($RMSE_z$) accuracies

The real coordinates (x, y, z) were obtained with GNSS system. These points were compared with the CP marked on the ground and observed in the digital model.

Figure 5 shows a map where planimetric and altimetric differences are observed in the generated DTM. Figure 5a shows a cross-section with a distance of 117 m, where a slope is observed. In this figure, three validation points are present: CP17, CP16 and CP14. The elevation differences observed between the DTM and GNSS measurements were less than 0.15 m. Figure 5b shows the horizontal errors in CP16. In this figure, the horizontal difference between the DTM and GNSS measurements was less than 0.02 m. Due to the differences found, equations (4) and (5) were used to obtain the planimetric ($RMSE_{xy}$) and altimetric ($RMSE_z$) accuracies for each photogrammetric survey.

3.6 Statistical analysis

A georeferencing process was implemented on the DTMs obtained. 27 GCP were used as georeferencing points and the accuracy of georeferenced DTMs was then evaluated using the 24 points that were established as CP. Table 5 shows the results of the plani-altimetric accuracy obtained in the eighteen surveys before and after the georeferencing process. The planimetric accuracy ($RMSE_{xy}$) before georeferencing process ranged from 9.01 to 1.46 m. This high variation was reduced after implementing the georeferencing process. $RMSE_{xy}$ after georeferencing ranged from 1.05 to 0.11 m. The same situation occurred for altimetric accuracy ($RMSE_z$). Lower values of $RMSE_z$ (higher altimetric accuracies) were registered after georeferencing. According to statistical analysis, when the georeferencing process was performed, a significant reduction in error was observed in both planimetric and altimetric accuracies ($p < 0.05$).

ANOVA was carried out to assess the effect of photogrammetric flight parameters on plani-altimetric accuracy of DTMs (Table 6). Based on statistical analysis performed, longitudinal overlap and flight mode were flight parameters that showed a significant influence on planimetric accuracy. According to main effect analysis,

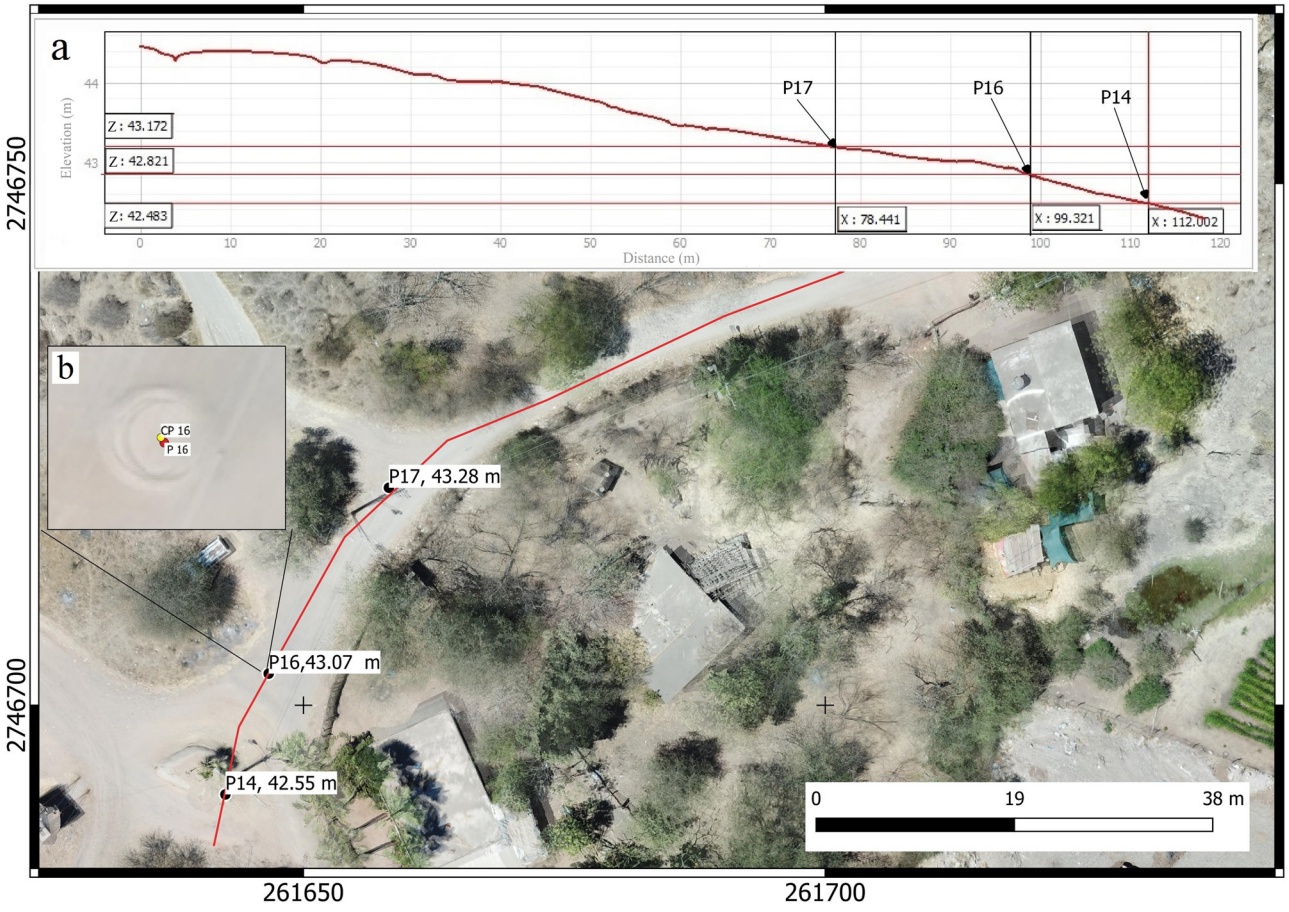

Figure 5: Planimetric and altimetric differences in the generated DTM. (a) Elevation differences observed in a cross-section. (b) Planimetric difference identified in GCP 16. Source: Own elaboration using QGIS 3.10 La coruña (Open Source Geospatial Foundation, Beaverton, USA, 2020).

lower $RMSE_{xy}$ values were registered when higher percentages of longitudinal overlap are used. Likewise, higher planimetric accuracies were observed when double grid flight mode was carried out.

Statistical analysis for altimetric accuracy showed that only the flight mode had a statistical significance ($p < 0.05$). Lower $RMSE_z$ values were observed in DTMs generated when double grid surveys were performed.

3.7 Optimization (the most accurate DTM generated)

According to statistical analysis, treatment 13 showed the highest plani-altimetric accuracy. Under these flight operational conditions, values of 0.38 and 0.11 m were achieved for $RMSE_{xy}$ and $RMSE_z$. In both cases, the digital models were adjusted by the georeferencing process using the GCP. In contrast, treatment 4 presented the lowest accuracy ($RMSE_{xy}$ = 1.05 m and $RMSE_z$ = 1.33 m). The resulting DTM shows neither artifacts nor unnatural terrain features, and it represents the real morphology of the terrain.

4 Discussion

4.1 Effect of the image overlapping

Figure 6 shows the amount of images that were overlapped in treatments 13 and 4. Treatment 4 generated with normal grid flight mode (Figure 6b) has a greater amount of red and yellow areas than the one generated with double grid (Figure 6a). The red and yellow zones are located mostly on the margins and these zones are characterized by the overlapping of one to three images. The green zones reflect that five or more

Table 5: Plani-altimetric accuracies obtained in all treatments

Treatment	DEM accuracy before georeferencing		DEM accuracy after georeferencing	
	$RMSE_{xy}$	$RMSE_z$	$RMSE_{xy}$	$RMSE_z$
1	1.46	14.64	0.80	0.75
2	1.92	8.88	0.71	0.49
3	9.01	15.15	0.59	0.97
4	2.71	32.51	1.05	1.33
5	2.03	27.45	0.63	1.57
6	2.44	27.28	0.58	0.67
7	6.75	29.00	1.04	1.06
8	1.66	26.2	0.79	0.89
9	1.74	24.12	0.83	0.63
10	4.34	17.45	0.51	0.41
11	3.71	3.07	0.96	0.61
12	6.72	7.39	0.97	0.92
13	3.00	3.59	0.11	0.38
14	3.88	11.07	0.13	0.35
15	5.51	5.31	0.90	1.02
16	3.90	2.87	0.20	0.40
17	6.19	7.09	0.41	0.62
18	4.13	10.52	0.27	0.44

Source: Own elaboration.

images were overlapped. Therefore, the DEM accuracy could be highly related to the amount of images overlapped, as it is suggested by Dandois et al. [50].

According to Mířijovský and Langhammer [33], the greater number of intersected photographs, the greater the precision in the 3D reconstruction process is. This situation is demonstrated in Figure 7, where lower $RMSE_z$ values were obtained when higher key points were identified (Figure 7a). Besides, higher altimetric accuracy was obtained when higher match points were correlated (Figure 7b). Altimetric accuracy was also correlated with the amount of frames. Treatments with a greater number of photographs (double grid) observed higher altimetric accuracies (Figure 7c). Therefore, the altimetric accuracy of a DEM depended on the densification points obtained during 3D reconstruction process, as it is also demonstrated in Zhao et al. [20].

In this study, high accuracy was achieved because images were acquired from different perspectives. However, it is important to determine the optimum overlap to achieve the desired accuracy without falling into long processing computation times. Altimetric precision must be optimized by balancing the number of intersected photographs. The stereoscopic multivision effect must be achieved taking into account the computational processing times. The greater the points correlate in a scattered point cloud, the denser the point cloud is generated with better detail and therefore greater accuracy.

Table 6: ANOVA and main effects of flight parameters on plani-altimetric accuracy

ANOVA for $RMSE_{xy}$		Main effects for $RMSE_{xy}$ (mean values)					
Flight parameter	***p*-Value**	**Flight mode**	**Mean $RMSE_{xy}$**	**Camera tilt**	**Mean $RMSE_{xy}$**	**Trans. overlap**	**Mean $RMSE_{xy}$**
Flight mode	0.014*	Normal	0.78	65°	0.62	60	0.63
Flight altitude (m)	0.156	Double	0.50	75°	0.61	70	0.77
Camera tilt (°)	0.522			85°	0.69	80	0.52
Long. overlap (%)	0.012*	Flight height	Mean $RMSE_{xy}$	Long. overlap	Mean $RMSE_{xy}$	Speed	Mean $RMSE_{xy}$
Trans. overlap (%)	0.169	60 m	0.76	40%	0.83	5 m/s	0.61
Flight speed	0.325	70 m	0.57	50%	0.62	7 m/s	0.58
*p-Values < 0.05 are significant		80 m	0.59	60%	0.47	9 m/s	0.72
ANOVA for $RMSE_z$		**Main effects for $RMSE_z$ (mean values)**					
Flight parameter	***p*-Value**	**Flight mode**	**Mean $RMSE_z$**	**Camera tilt**	**Mean $RMSE_z$**	**Trans. overlap**	**Mean $RMSE_z$**
Flight mode	0.028*	Normal	0.93	65°	0.73	60	0.65
Flight altitude (m)	0.441	Double	0.58	75°	0.76	70	0.85
Camera tilt (°)	0.766			85°	0.78	80	0.77
Long. overlap (%)	0.224	Flight height	Mean $RMSE_z$	Long. overlap	Mean $RMSE_z$	Speed	Mean $RMSE_z$
Trans. overlap (%)	0.402	60 m	0.69	40%	0.83	5 m/s	0.71
Flight speed	0.138	70 m	0.89	50%	0.81	7 m/s	0.61
*p-Values < 0.05 are significant		80 m	0.68	60%	0.62	9 m/s	0.94

Source: Own elaboration using Statgraphics Centurion 18 (Statgraphics Inc., The Plains, USA, 2020).

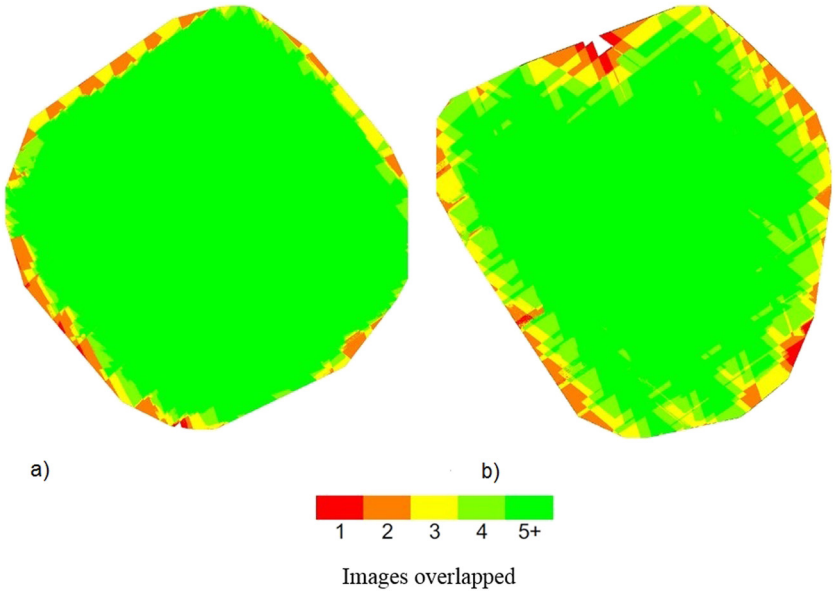

Figure 6: Images overlapped in DEMs generated in treatments 13 and 4. Source: Own elaboration using Pix4D (Pix4D SA, Laussane, Switzerland, 2011). (a) Overlapped images in treatment 13, (b) overlapped images in treatment 4.

4.2 Effect of the georeferencing process

The effect of the georeferencing process on the plani-altimetric accuracy of the DTM is shown in Figure 8. Plani-altimetric accuracy is strongly dependent on this georeferencing process. The Box and Whisker plot shows the planimetric (Figure 8a) and altimetric (Figure 8b) accuracies before and after georeferecing process. In general, a high error is observed in the DTMs generated before georeferencing. According to the results obtained in this study, georeferencing is a critical process for improving the accuracy of DTMs. Therefore, technological alternatives must be developed for the georeferencing process. The complexity of terrestrial areas and the extensive time consuming for the establishment of GCPs on the ground represent a major opportunity area in RPAS photogrammetry. The georeferencing process is being integrated as an indirect system on the RPAS [51]. In the future, this situation will replace the use of GCPs.

Luhmann et al. [52] suggest the use of at least 20 GCPs to achieve high precision in DEMs. In this study, 27 GCPs were considered for georeferencing. Few studies are given about the effect of the georeferencing process in DEM accuracy. More in-depth studies are needed to determine the optimal amount of GCPs that must be used for the generation of DEMs with high accuracy.

4.3 Effect of the photogrammetric flight parameters

Planimetric accuracy results varied from 0.11 to 1.05 m. The planimetric accuracies obtained are similar to the results obtained in other photogrammetric studies. Seifert et al. [53] reported a planimetric accuracy range of 0.10 to 0.15 m, while Matthews [54] reported a planimetric accuracy of 0.08 to 0.40 m. These high planimetric accuracy results were obtained using double grid flight. This coincides with the result reported by Zhao et al. [20], who found that double and triple overlapping concentrate a large number of intersected pixels, which increased the planimetric accuracy of DEM. The stereoscopic multivision and 360° perspective given by the multiple intersections of photographs increased DEM accuracy. SfM algorithms showed a better result when high redundancy block configuration was performed. A higher correlation of overlapping characteristics in multiple photographs was observed under these conditions.

Rabah et al. [51] suggest implementing a high longitudinal overlap, but also a high vertical overlap to obtain high DEM accuracy. In particular, Westoby et al. [55] and Eisenbeiss [56] report that high percentages of longitudinal and transversal overlaps result in low RMSE. However, the results obtained in this work

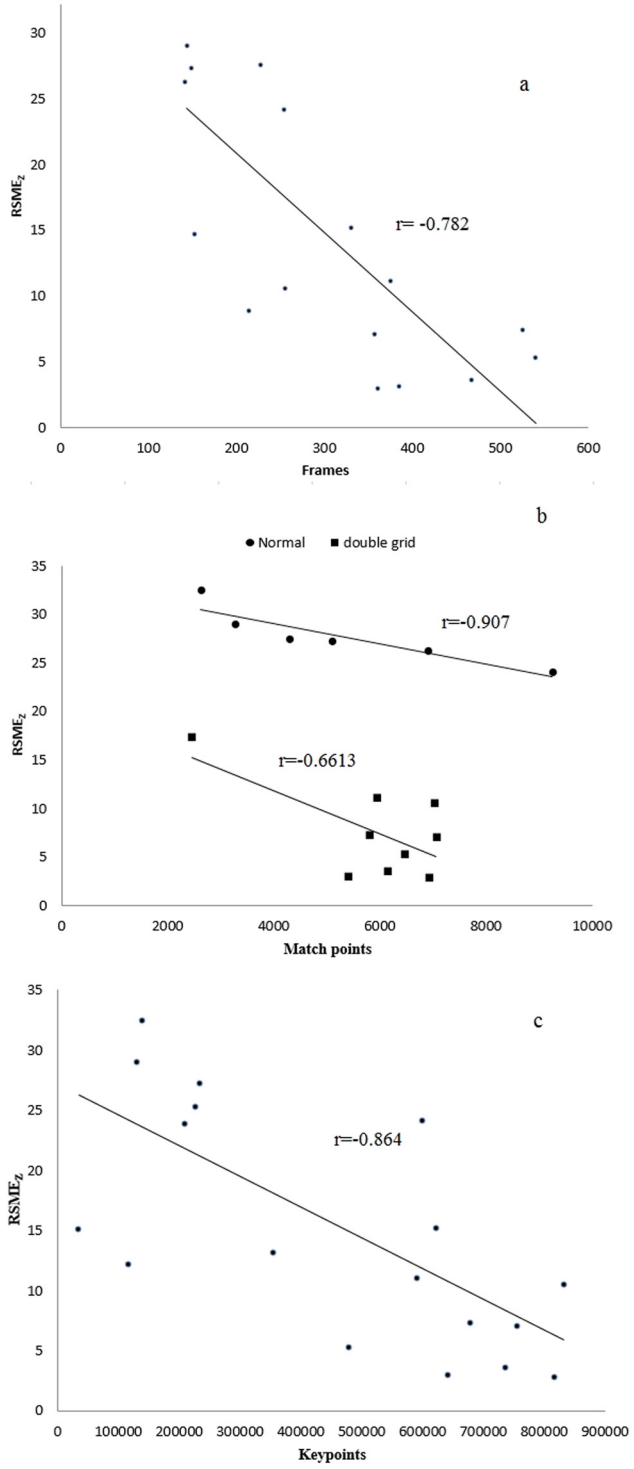

Figure 7: Relationship between altimetric accuracy and 3D reconstruction process. (a) Correlation between altimetric accuracy and keypoints identified. (b) Correlation between altimetric accuracy and matched points. (c) Correlation between altimetric accuracy and frames acquired. Source: Own elaboration using Statgraphics Centurion 18 (Statgraphics Inc., The Plains, USA, 2020).

indicated that the transversal overlap did not have a significant effect on planimetric accuracy ($p > 0.05$).

Flight altitudes of 30, 40, 50, 60, 70 and 80 m were set for the production of orthomosaics for archaeological applications in the study by Mesas-Carrascosa et al. [39] and they concluded that flight altitude is the main flight parameter because of its influence on $RMSE_{xy}$. However, in this study, low flight altitudes (<60 m) were discarded because this implied the processing of a high amount of images and consequently, high computation times. Flight altitudes of 60, 70 and 80 m were established for photogrammetric surveys and no significant effect was found on $RMSE_{xy}$ ($p > 0.05$). Mesas-Carrascosa et al. [39] also suggested that camera angle close to nadir (90°) is required to obtain high planimetric accuracy. This study demonstrated that the camera tilt was not a significant flight parameter for planimetric accuracy ($p > 0.05$).

Some studies have suggested that certain configurations are determinant for altimetric accuracy. Henriques et al. [57] suggested that transversal overlap has a significant influence on the density of the point cloud created for DEM generation. However, the results obtained in this research indicate that transversal overlap was not statistically significant on altimetric accuracy ($p > 0.05$).

Rabah et al. [51] report that the nadir view (90°) generates many occlusions in the image data set. According to Dandois et al. [50], steep hills, natural or artificial constructions, such as walls or buildings, generate hidden areas in the images. Both studies suggest that this effect could be reduced with the camera tilt or with a greater GSD. In this study, the statistical analysis (ANOVA) demonstrated that the camera tilt did not have any significant effect on the DTM accuracy ($p > 0.05$). However, in our study, a greater DTM accuracy was observed when surveys were carried out with great obliquity (65°).

Likewise, Torres-Sánchez et al. [58] indicate that high flight altitudes resulted in deterioration of DEM accuracy. In this study, altimetric accuracy was not influenced by the flight altitude ($p > 0.05$). According to statistical analysis, double grid flight was the unique determinant flight parameter for altimetric accuracy. The altimetric accuracy obtained in this study could be considered as high, according to the Udin and Ahmad's report [59], who reported altimetric accuracies ranging from 0.045 to 0.52 m for DEM generation.

4.4 Field validation

The performance of the optimum flight parameters was evaluated in different topographical conditions. Culiacan

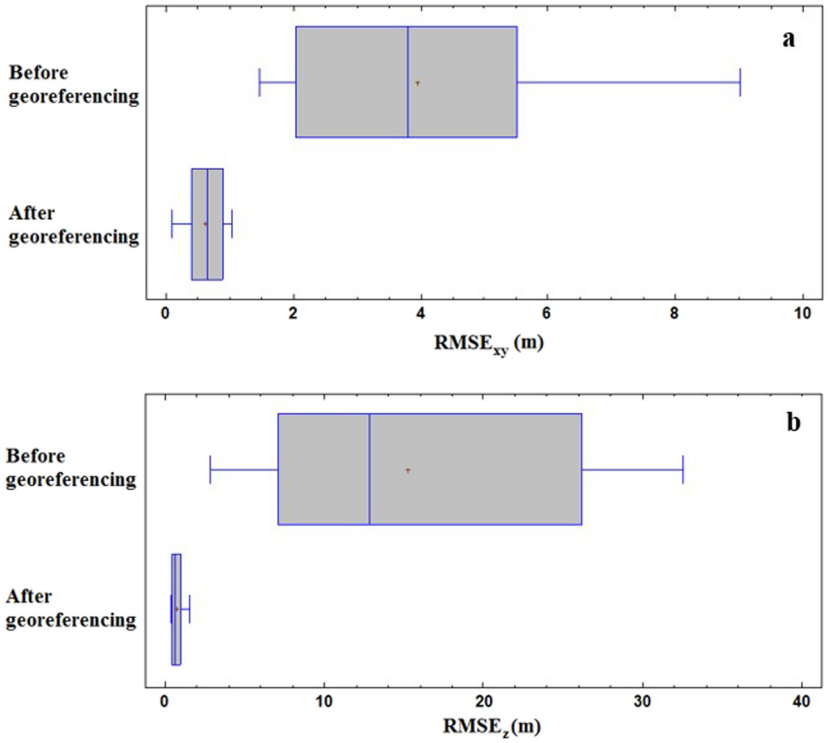

Figure 8: Box and Whisker plots showing the importance of georeferencing process on the DTM accuracy. (a) The effect of georeferencing onplanimetric accuracy. (b) The effect of georeferencing on altimetric accuracy. Source: Own elaboration using Statgraphics Centurion 18 (Statgraphics Inc., The Plains, USA, 2020).

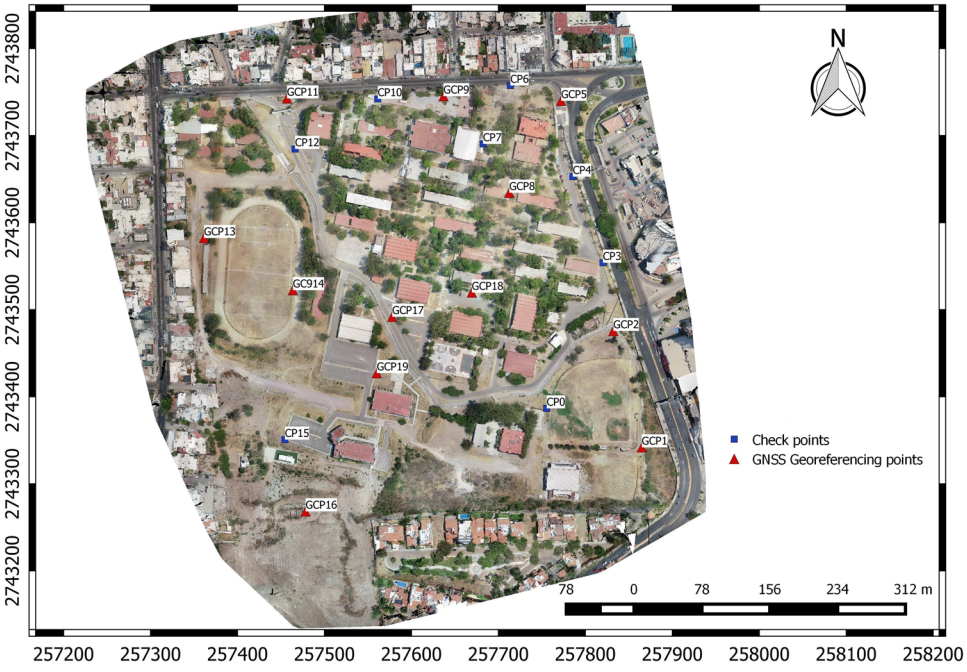

Figure 9: GCPs and CPs established for DEM validation at Culiacan Institute of Technology. Source: Own elaboration using QGIS 3.10 La coruña (Open Source Geospatial Foundation, Beaverton, USA, 2020).

Table 7: Comparison between DTM and CPs coordinates obtained for plani-altimetric accuracy during validation

Point number	DTM coordinates			CP coordinates			Difference (m)		
	X_{DTM}	Y_{DTM}	Z_{DTM}	X_{CP}	Y_{CP}	Z_{CP}	X_{DIF}	Y_{DIF}	Z_{DIF}
0	257478.27	2743268.2	83.08	257478.27	2743268.2	83.01	0.00	−0.01	0.07
1*	257454.50	2743350.6	69.85	257454.51	2743350.6	69.85	−0.01	−0.02	0.00
2*	257560.20	2743427.1	62.75	257560.19	2743427.1	62.50	0.01	0.00	0.25
3	257577.91	2743491.8	59.99	257577.90	2743491.9	59.15	0.01	−0.03	0.84
4	257669.43	2743519.7	62.37	257669.42	2743519.7	62.24	0.01	0.00	0.13
5*	257463.66	2743522.4	58.86	257463.65	2743522.4	58.75	0.01	0.00	0.11
6	257361.43	2743582.3	59.84	257361.41	2743582.3	59.20	0.02	0.00	0.64
7	257466.15	2743684.6	57.51	257466.25	2743684.5	57.15	−0.10	0.09	0.36
8*	257456.88	2743742.7	55.50	257456.85	2743742.7	55.45	0.03	0.02	0.05
9*	257561.26	2743742.2	59.44	257561.25	2743742.2	59.15	0.01	0.01	0.29
10	257636.88	2743745.2	61.93	257636.86	2743745.3	61.65	0.02	−0.01	0.28
11*	257713.77	2743757.5	64.96	257713.77	2743757.6	64.55	0.00	−0.01	0.41
12	257772.19	2743739.9	68.57	257772.18	2743739.9	68.05	0.01	0.00	0.52
13*	257785.62	2743652.8	67.22	257785.58	2743652.8	66.55	0.04	−0.02	0.67
14*	257712.54	2743634.3	65.25	257712.55	2743634.3	65.05	−0.01	0.00	0.20
15	257682.38	2743690.5	64.64	257682.38	2743690.5	64.21	0.00	0.00	0.43
16*	257820.25	2743553.9	67.23	257820.23	2743553.9	67.10	0.02	0.00	0.23
17*	257832.23	2743475.5	64.77	257832.22	2743475.5	65.12	0.01	−0.01	−0.35
18*	257864.94	2743341.8	67.72	257864.93	2743341.8	67.56	0.01	0.00	0.16
19*	257755.61	2743386.5	65.12	257755.60	2743386.6	64.90	0.01	−0.02	0.22

*GCPs used for georeferencing. Source: Own elaboration. Coordinates extracted from QGIS (Open Source Geospatial Foundation, Beaverton, USA, 2020).

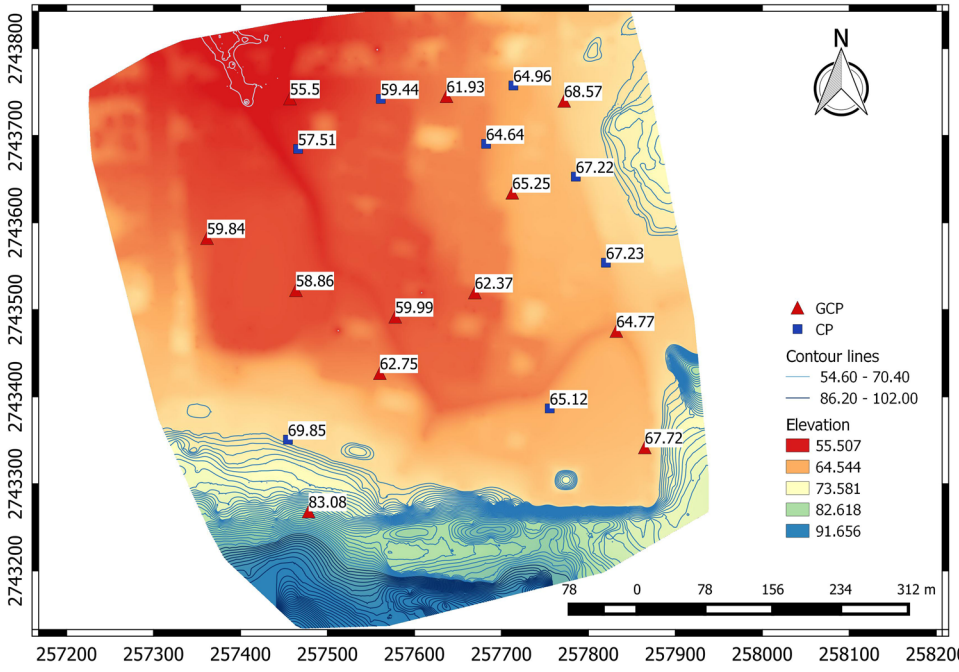

Figure 10: Contour lines and DTM generated during field validation. Source: Own elaboration using QGIS 3.10 La coruña (Open Source Geospatial Foundation, Beaverton, USA, 2020).

Institute of Technology was chosen since it is a terrain with steeper slopes (more than 50%). Figure 9 shows a distributed regular network of 20 GCPs, of which 12 GCPs were designated for georeferencing (indicated with asterisk in Table 7) and 8 GCPs designated for DTM validation. These points were marked on the ground to be easily distinguished from the background during the processing of the aerial images. The entire methodology proposed in this study was used for image acquisition, data processing, and DTM validation.

According to Table 7, the $RMSE_z$ and $RMSE_{xy}$ obtained were 0.37 and 0.05 m, respectively. These results were very similar to those obtained for DTM generated for Tamazula river. Figure 10 shows the DTM generated for Culiacan Institute of Technology. In analytical and modern photogrammetry performed with manned aircraft, the elevations in a study area should not vary 5% with respect to the flight altitude [60]. According to this criterion, the scale differences (GSD) in the images must not affect the accuracy of the final digital model. In the field validation, DTM elevation ranged from 54 to −102 m. In this sense, the methodology proposed in our study was validated and can be used in different zones with different topography, in particular in areas with steeper slopes. However, the methodology proposed must also be evaluated in areas with high vegetation density [61]. Knowing the importance of the vegetation density on the methodology proposed and the digital model generated is an opportunity area identified in our study.

5 Conclusions

This research provides a low-cost, high precision and easy-to-operate DEM acquisition and construction methodology using RPAS photogrammetry, useful for regions where there are no sufficient resources to develop this type of cartographic products. The DTM accuracy obtained could demonstrate that the methodology proposed can be comparable with other technologies that are expensive and require high knowledge and experience for their operation. The methodology proposed standardized all phases of DEM generation, from the acquisition of images by using RPAS to DEM construction, considering the best available algorithm for image processing.

By using a Taguchi orthogonal array L_{18}, 18 surveys were carried out to evaluate six different flight parameters and to figure out the optimal conditions that a photogrammetric flight should be programmed for generating a DTM with high plani-altimetric accuracy. This methodology generated a set of georeferenced and non-georeferenced models; the results indicate that the georeferencing process normalized all the models and generated models with a similar high plani-altimetric accuracy. This study demonstrated a significant variation reduction when this process is included as part of the methodology for DEM generation. The georeferencing process is especially important as it invalidates the effect of almost every flight parameter considered in the DEM methodology construction.

This study also demonstrated that flight mode had a statistical effect on both planimetric and altimetric accuracies of DTM. In particular, this study suggests that double grid surveys generated DTMs with higher plani-altimetric accuracy. In addition, planimetric accuracy was influenced by the longitudinal overlap. The results suggested a high longitudinal overlap (at least 60%) to achieve high planimetric accuracy.

Acknowledgments: This research was funded by CONACYT, Mexico, Cátedras 2014 Ref. 2572. Authors acknowledge the support given by Culiacan Institute of Technology for the construction of the Remote Sensing Lab.

Limitations: This study proposes an RPAS flight configuration for the generation of DTM with high precision and accuracy. A quadcopter was used to perform low altitude flights, where terrain elevation variations are minimal in comparison to the ones observed in rugged mountains. In addition, quadcopter flights have limited battery capacity. Therefore, the use of an autonomous battery recharging and swapping system is suggested for longer flight times and to cover larger areas.

Further research: Digital models generated in this study could be used for hydrological modeling. The recent literature demonstrates that hydrological modeling is carried out by using low-resolution satellite images, with errors ranging from 1 to 5 m. The use of high-resolution digital models could generate hydrological scenarios with millimeter precision. In this sense, the methodology proposed could be considered as an alternative technology useful for the development of risk mitigation strategies (i.e., in flood risk areas).

Conflict of interest: The authors declare no conflict of interest.

References

[1] Zweig CL, Burgess MA, Pecival HF, Kitchens WM. Use of unmanned aircraft systems to delineate fine-scale wetland vegetation communities. Wetlands. 2015;35:303–9.

[2] Lane SN, Chandler JH, Porfiri K. Monitoring river channel and flume surfaces with digital photogrammetry. J Hydraul Eng. 2001;127:871–7.

[3] Javernick L, Brasington J, Caruso B. Modeling the topography of shallow braided rivers using structure-from-motion photogrammetry. Geomorphology. 2014;213:166–82.

[4] Brasington J, Vericat D, Rychkov I. Modeling river bed morphology, roughness, and surface sedimentology using high resolution terrestrial laser scanning. Water Resour Res. 2012;48:1–18.

[5] Devereux B, Amable G. Airborne LiDAR: instrumentation, data acquisition and handling. In: Heritage GL, Large ARG. Laser Scanning for the Environment Sciences, vol. 4, 1st edn. Hoboken, USA: Blackwell Publishing Ltd; 2009. p. 49–66.

[6] Hugenholtz CH, Whitehead K, Brown OW, Barchyn TE, Brian JM, LeClair A, et al. Geomorphological mapping with a small unmanned aircraft system (sUAS): feature detection and accuracy assessment of a photogrammetrically-derived digital terrain model. Geomorphology. 2013;1946:16–24.

[7] Shahbazi M, Sohn G, Théau J, Menard P. Development and evaluation of a UAV-photogrammetry system for precise 3D environmental modeling. Sensors. 2015;15:27493–524.

[8] Uysal M, Toprak AS, Polat N. DEM generation with UAV photogrammetry and accuracy analysis in Sahitler hill. Measurement. 2015;73:539–43.

[9] Eltner A, Kaiser A, Abellan A, Schindewolf M. Time lapse structure-from-motion photogrammetry for continuous geomorphic monitoring. Earth Surf Process Landf. 2017;42:2240–53.

[10] Clapuyt F, Vanacker V, Van Oost K. Reproducibility of UAV-based earth topography reconstructions based on structure-from-motion algorithms. Geomorphology. 2016;260:4–15.

[11] Leitão JP, de Vitry Moy, Scheidegger M, Rieckermann AJ. Assessing the quality of digital elevation models obtained from mini unmanned aerial vehicles for overland flow modelling in urban areas. Hydrol Earth Syst Sci. 2016;20:1637–53.

[12] Nouwakpo SK, Weltz MA, McGwire K. Assessing the performance of structure-from-motion photogrammetry and terrestrial LiDAR for reconstructing soil surface microtopography of naturally vegetated plots: SfM and LiDAR performance on vegetated plots. Earth Surf Process Landf. 2015;4:308–22.

[13] Colomina I, Molina P. Unmanned aerial systems for photogrammetry and remote sensing: a review. ISPRS J Photogramm Remote Sens. 2014;92:79–97.

[14] Gabrlik P, Vomocil J, Zalud L. The design and implementation of 4 DOF control of the quadrotor. In: 2013 12th IFAC Conference on Programmable Devices and Embedded Systems, vol. 46; 2013. p. 68–73.

[15] Lopez-Gutierrez R, Rodriguez-Mata A, Salazar S, Gonzalez-Hernandez I, Lozano R. Robust quadrotor control: attitude and altitude real-time results. J Intell Robot Syst. 2017;88:299–312.

[16] Hirschmüller H. Stereo processing by semiglobal matching and mutual information. IEEE Trans Pattern Anal Mach Intell. 2008;30:328–41.

[17] Smith MW, Carrivick JL, Quincey DJ. Structure from motion photogrammetry in physical geography. Prog Phys Geogr. 2016;40:247–75.

[18] Barazzetti L, Brumana R, Oreni D, Previtali M, Roncoroni F. True-orthophoto generation from UAV images: implementation of a combined photogrammetric and computer vision approach. ISPRS Ann Photogramm Remote Sens Spat Inf Sci. 2014;II-5:57–63.

[19] Harwin S, Lucieer A. Assessing the accuracy of georeferenced point clouds produced via multi-view stereopsis from unmanned aerial vehicle (UAV) imagery. Remote Sens. 2012;4:1573–99.

[20] Zhao H, Zhang B, Shang J, Lui J. Aerial photography flight quality assessment with GPS/INS and DEM data. ISPRS J Photogramm. 2018;135:60–73.

[21] Fonstad MA, Dietrich JT, Courville BC, Jensen JL, Carbonneau P. Topographic structure from motion: a new development in photogrammetric measurement. Earth Surf Process Landf. 2013;38:421–30.

[22] Furukawa Y, Curless B, Seitz S, Szeliski R. Towards Internet-scale multiview stereo. In: 2010 IEEE Computer Society Conference on Computer Vision and Pattern Recognition. San Francisco, CA, USA, 13–18, June 2010. USA: IEEE; 2010.

[23] Marteau B, Vericat D, Gibbins C, Batalla R, Green D. Application of structure-from-motion photogrammetry to river restoration. Earth Surf Process Landf. 2016;42:503–15.

[24] Rentería-Guevara SA, Sanhouse-García A, Bustos-Terrones Y, Rodriguez-Mata AE, Rangel-Peraza JG. A proposal to integrate the legal definition and official delineation of watersheds in Mexico: eight model case studies. Rev Ambient Água. 2019;14:1–21.

[25] Hussain M, Bethel J. Photogrammetric project and mission planning. In: McGlone JC, Lee GYG. Manual of Photogrammetry, vol. 15, 6th edn. Bethesda, USA: AAPRS; 2013. p. 1187–220.

[26] Reshetyuk Y, Mårtensson S. Generation of highly accurate digital elevation models with unmanned aerial vehicles. Photogram Rec. 2016;31:143–65.

[27] Dall'Asta E, Forlani G, Roncella R, Santise M, Diotri F, Morra di Cella U. Unmanned aerial systems and DSM matching for rock glacier monitoring. ISPRS J Photogramm. 2017;127:102–14.

[28] Wasklewicz T, Staley DM, Reavis K, Oguchi T. Digital terrain modeling. In: Bishop MP, editor. *Treatise on Geomorphology*, *Volume 3*, London, UK: Academic Press; 2013. p. 130–61.

[29] Bemis S, Micklethwaite S, Turner D, James MR, Akciz S, Thiele S, et al. Ground-based and UAV-based photogrammetry: a multiscale, high-resolution mapping tool for structural geology and paleoseismology. J Struct Geol. 2014;69:163–78.

[30] Mora-Felix ZD, Rangel-Peraza JG, Sanhouse-Garcia AJ, Flores-Colunga GR, Rodríguez-Mata AE, Bustos-Terrones YA. The use of RPAS for the development of land surface models for natural resources management: a review. Interdiscip Environ Rev. 2018;19:243–65.

[31] Pajares G. Overview and status of remote sensing applications based on unmanned aerial vehicles (UAVs). Photogramm Eng Rem S. 2015;81:281–330.

[32] Vollgger SA, Cruden AR. Mapping folds and fractures in basement and cover rocks using UAV photogrammetry, Cape Liptrap and Cape Paterson, Victoria, Australia. J Struct Geol. 2016;85:168–87.
[33] Mířijovský J, Langhammer J. Multitemporal monitoring of the morphodynamics of a mid-mountain stream using UAS photogrammetry. Remote Sens. 2015;7:8586–609.
[34] Pei H, Wan P, Li C, Feng H, Yang G, Xu B, et al. Accuracy analysis of UAV remote sensing imagery mosaicking based on structure-from-motion. In: 2017 IEEE International Geoscience and Remote Sensing Symposium (IGARSS). Fort Worth, USA, 23–28 July 2017. USA: IEEE; 2017. p. 5904–7.
[35] Nex F, Remondino F. UAV for 3D mapping applications: a review. Appl Geomat. 2013;6:1–15.
[36] Fraser C. Automatic camera calibration in close range photogrammetry. Photogramm Eng Rem S. 2013;79:381–8.
[37] Turner D, Lucieer A, Wallace L. Direct georeferencing of ultrahigh-resolution UAV imagery. IEEE Trans Geosci Remote Sens. 2014;52:2738–45.
[38] Lowe DG. Object recognition from local scale-invariant features. In: Proceedings of the Seventh IEEE International Conference on Computer Vision, Kerkyra, Greece, 20–27 Sept. 1999, vol. 2. Greece: IEEE; 1999. p. 1150–7.
[39] Mesas-Carrascosa F, Notario García M, Meroño de Larriva J, García-Ferrer A. An analysis of the influence of flight parameters in the generation of unmanned aerial vehicle (UAV) orthomosaicks to survey archaeological areas. Sensors. 2016;16:1838.
[40] Zhou L, Yang X. Training algorithm performance for image classification by neural networks. Photogramm Eng Remote Sens. 2010;8:945–51.
[41] Turner D, Lucieer A, Watson C. An automated technique for generating georectified mosaics from ultra-high resolution unmanned aerial vehicle (UAV) imagery, based on structure from motion (SfM) point clouds. Remote Sens. 2012;4:1392–410.
[42] Hirschmüller H. Accurate and efficient stereo processing by semi-global matching and mutual information. In: IEEE Computer Society Conference on Computer Vision and Pattern, 20–25 June 2005; San Diego, USA, volume 2. USA: IEEE; 2005. p. 807–14.
[43] Legrá-Lobaina AA, Atanes-Beaton DM, Guilarte-Fuentes C. Contribución al método de interpolación lineal con triangulación de Delaunay. Min Geol. 2014;30:58–72.
[44] Sanhouse-Garcia A, Bustos-Terrones Y, Rangel-Peraza J, Quevedo-Castro A, Pacheco C. Multi-temporal analysis for land use and land cover changes in an agricultural region using open source tools. Remote Sens Appl Soc Environ. 2017;8:278–90.
[45] Kazhdan M, Bolitho M, Hoppe H. Poisson surface reconstruction. In: Polthier K, Sheffer A, editors. Proceedings of the fourth Eurographics symposium on Geometry processing, Cagliari, Italy, 26–28 June, 2006. Aire-la-Ville, Switzerland: Eurographics Asociation; 2006. p. 61–70.
[46] Unger M, Pock T, Grabner M, Klaus A, Bischof H. A variational approach to semiautomatic generation of digital terrain models. In: 5th International Symposium on Visual Computing, Las Vegas, USA, 30 November–2 December 2009, vol. 5876. Berlin, Germany: Springer; 2009. p. 1119–30.
[47] Smith MW, Vericat D. From experimental plots to experimental landscapes: topography, erosion and deposition in sub-humid badlands from structure-from-motion photogrammetry. Earth Surf Process Landf. 2015;40:1656–71.
[48] Aguilar FJ, Aguilar MA, Agüera F. Accuracy assessment of digital elevation models using a non-parametric approach. Int J Geogr Inf Sci. 2007;21:667–86.
[49] Wang B, Shi W, Liu E. Robust methods for assessing the accuracy of linear interpolated DEM. Int J Appl Earth Obs Geoinf. 2015;34:198–206.
[50] Dandois JP, Olano M, Ellis EC. Optimal altitude, overlap, and weather conditions for computer vision UAV estimates of forest structure. Remote Sens. 2015;7:13895–920.
[51] Rabah M, Basiouny M, Ghanem E, Elhadary A. Using RTK and VRS in direct geo-referencing of the UAV imagery. NRIAG J Astron Geophys. 2018;7:220–6.
[52] Luhmann T, Fraser C, Maas H-G. Sensor modelling and camera calibration for close-range Photogrammetry. ISPRS J Photogramm Remote Sens. 2016;115:37–46.
[53] Seifert E, Seifert S, Vogt H, Drew D, van Aardt J, Kunneke A, et al. Influence of drone altitude, image overlap, and optical sensor resolution on multi-view reconstruction of forest images. Remote Sens. 2019;11:1252.
[54] Matthews NA. Aerial and close-range photogrammetric technology: providing resource documentation, interpretation, and preservation. Technical Note 428. Denver, Colorado, USA: US Department of the Interior, Bureau of Land Management; 2008. p. 42.
[55] Westoby MJ, Brasington J, Glasser NF, Hambrey MJ, Reynolds JM. Structure-from-motion photogrammetry: a low-cost, effective tool for geoscience applications. Geomorphology. 2012;179:300–14.
[56] Eisenbeiss H. UAV Photogrammetry [Doctor of Sciences Thesis]. Desden, Germany: University of Technology Dresden; 2009. p. 2009.
[57] Henriques M, Fonseca A, Roque D, Lima J, Marnoto J. Assessing the quality of an UAV-based orthomosaic and surface model of a breakwater. In: Proceedings of FIG Congress 2014, Kuala Lumpur, Malaysia, 16–21 June 2014. New Delhi, India: Coordinates; 2014. p. 1–16.
[58] Torres-Sánchez J, López-Granados F, Borra-Serrano I, Peña JM. Assessing UAV-collected image overlap influence on computation time and digital surface model accuracy in olive orchards. Precis Agric. 2018;19:115–33.
[59] Udin W, Ahmad A. Assessment of photogrammetric mapping accuracy based on variation flying altitude using unmanned aerial vehicle. IOP Conf Ser Earth Environ Sci. 2014;18: 012027.
[60] Lerma J. Fotogrametria moderna: analitica y digital. Spain: Universitat Politécnica de Valéncia Publishers; 2002.
[61] Aktürk E, Altunel A. Accuracy assessment of a low-cost UAV derived digital elevation model (DEM) in a highly broken and vegetated terrain. Measurement. 2018;136:382–6.
[62] Wu C. Visual SFM, A Visual Structure from Motion System. 2011, http://www.cs.washington.edu/homes/ccwu/vsfm/.